# *Supporting Information for*

**Vertical Gradient in Atmospheric Particle Phase State: A Case Study Over the Alaskan Arctic Oil Fields**

Nurun Nahar Lata[1], Zezhen Cheng[1], Darielle Dexheimer[2], Susan Mathai[1,3], Matthew A. Marcus[4], Kerri A. Pratt[5], Theva Thevuthasan[1], Fan Mei[6], Swarup China[1, *]

[1] Environmental Molecular Sciences Laboratory, Pacific Northwest National Laboratory, Richland, WA 99354, USA

[2] Sandia National Laboratory, Albuquerque, NM 87123, USA

[3] Michigan Technological University, Houghton, MI, 49931, USA

[4] Advanced Light Source, Lawrence Berkeley Lab, Berkeley, California 94720 USA

[5] Department of Chemistry and Department of Earth and Environmental Science University of Michigan, Ann Arbor, MI 48109, USA

[6] Atmospheric, Climate, & Earth Sciences Division, Pacific Northwest National Laboratory, Richland, WA 99352, USA

[*]Corresponding author: Swarup China, Swarup.China@pnnl.gov; +1 509 371-7329

**TABLE OF CONTENT**

**Single-particle analysis**

We used an environmental scanning electron microscope (SEM) in computer-controlled mode to image single particles (ESEM, Quanta 3D, Thermo Fisher). To measure elemental composition, the SEM is connected to an energy-dispersive X-ray (EDX) spectrometer with a Si (Li) detector that has an active surface area of 10 $mm^2$. The X-ray spectra were taken with a beam current of 0.48 nA and an accelerating voltage of 20 kV. The program automatically finds particles and determines shape properties, such as the area they project and their aspect ratio. Once a single particle was found, an EDX spectrum was taken and measured so that the relative amounts of 16 elements (C, N, O, Na, Mg, Al, Si, P, S, Cl, K, Ca, Mn, Fe, Zn, and Cu) could be found. The Cu signal in the EDX spectrum is caused mostly by the substrate (copper transmission electron microscope grids) and the beryllium–copper alloy mounting plate that holds the sample inside the instrument. CCSEM/EDX data on atomic percentages then were sorted according to the particle sorting scheme shown in Figure S1. Based on the amount of each element (measured as atomic%), we grouped the particles into the following eight categories[1]: 1) Na-rich, 2) Na-rich/sulfate, 3) Carbonaceous sulfate-rich, 4) carbonaceous-rich, 5) dust, 6) carbonaceous rich dust 7) sulfate rich dust, and 8) other. First, particles with more/less than 1 atomic% Na were divided into two classes. Because aerosol particles were collected near maritime environments, they are Na-rich or Na-lean. Because dust particles contain Al, Si, Fe, and Ca, Na-rich particles were classified into two groups based on their mineral element abundance. Particles having more Na than mineral elements (Al, Si, Fe, and Ca) were classified as "Na-rich" ([Na] ≥[S]) or "Na-rich/Sulfates" ([Na] <[S]) based on S concentration relative to Na. Sodium-deficient particles ([Na] <1 atomic %) were categorized into four types. Carbonaceous particles are C, N, and O-dominated particles (>99 atomic%). Particles with S concentrations exceeding 0.5 atomic% were categorized as "sulfate" when C, N, O, and S were the predominant constituent elements (>99 atomic%). Dust had (Al, Si, Fe, Ca) exceeding 4 atomic%. Two groups were created for particles with (Al, Si, Fe, Ca) <4 atomic%. Particles with Al, Si, Fe, Ca amounts >2% were separated into two classes: carbonaceous rich dust with [C, N, O] greater than 85 atomic% and sulfate rich dust with [S]>1%. A particle that does not match the above criteria is classified as "other."

Scanning transmission X-ray microscopy with near-edge X-ray absorption fine structure spectroscopy (STXM/NEXAFS) was used to study the carbon features in the aerosol population. Details of the STXM/NEXAFS available at the Advanced Light Source beamline at Lawrence Berkeley National Laboratory have been described before[2]. Through transmission of synchrotron light beams from a synchrotron light source across raster-scanned samples at predetermined photon energies, scientists can study chemical bonds between elements. To get X-ray absorption spectra of the carbon K-edge, particles with energies between 278 and 320 eV were scanned. To get an optical density ($OD_E$), we first use the Beer-Lambert Law to change the X-rays that the particles give off at each energy and position:

$$OD_E = -\ln\left(\frac{I(E)}{I_o(E)}\right) = \mu(E)\rho t \quad (S1)$$

Where $I$ is the intensity at a given energy, $I_o$ is the background intensity, $\mu(E)$ is the mass absorption coefficient at X-ray energy E, $\rho$ is the mass density and $t$ is the particle thickness[3].

"Stacks" of the carbon K-edge spectrum were taken at 111 different energy levels, while "maps" were taken at 11 different energy levels. Space-resolved spectra were used to figure out the carbon content and mixing state of each particle. For the STXM imaging, a 25 nm zone plate was used[4,5]. STXM data are used to evaluate different types of internally mixed particles, such as organic carbon (OC) where the organic mass is evenly distributed throughout the particle, elemental carbon mixed with organic carbon (EC+OC) where particles have higher C=C, $sp^2$ hybridized bonds and organic functionalities, organic carbon mixed with inorganics (IN+OC), and particles with mixtures of organic carbon, elemental carbon, and inorganic inclusion (OC+EC+IN+OC)[3,6].

The carbon K-edge images can be used to calculate the organic volume fraction (OVF)[7]. The thickness of both organic and inorganic components was calculated from the optical density at energy either pre-edge (278 eV) or post-edge (320eV). The OD at each a given energy can be estimated as a linear combination of the ODs of the inorganic and organic components[7,8] -

$$OD_{278} = \mu_{278}^{IN}\rho^{IN}t^{IN} + \mu_{278}^{ORG}\rho^{ORG}t^{ORG} (S2)$$

$$OD_{320} = \mu_{320}^{IN}\rho^{IN}t^{IN} + \mu_{320}^{ORG}\rho^{ORG}t^{ORG} (S3)$$

where INO and ORG representing inorganic and organic components. By taking $OD_{320}$-$OD_{278}$, the thickness of the inorganic ($t^{IN}$) and organic ($t^{ORG}$) components can be calculated as:

$$t^{IN} = \frac{OD_{278} - \mu_{278}^{ORG}\rho^{ORG}t^{ORG}}{\mu_{278}^{IN}\rho^{IN}} \quad (S4)$$

$$t^{ORG} = \frac{OD_{320} - A^{IN}OD_{278}}{\left(\mu_{320}^{ORG} - A^{IN}\mu_{278}^{ORG}\right) \times \rho^{ORG}} \quad (S5)$$

where, $A^{IN}$ is $\frac{\mu_{320}^{IN}}{\mu_{320}^{ORG}}$ .Then the OVF was calculated by taking the ratio of the organic component thickness to the total thickness. The mass absorption coefficients were calculated using previous methods[9]. The densities and mass absorption coefficient of $(NH_4)_2SO_4$ (1.77 g $cm^{-3}$) and adipic acid (1.36 g $cm^{-3}$) are used for this work. The $OD_{320}$-$OD_{278}$ was used to calculate the TCA[10].

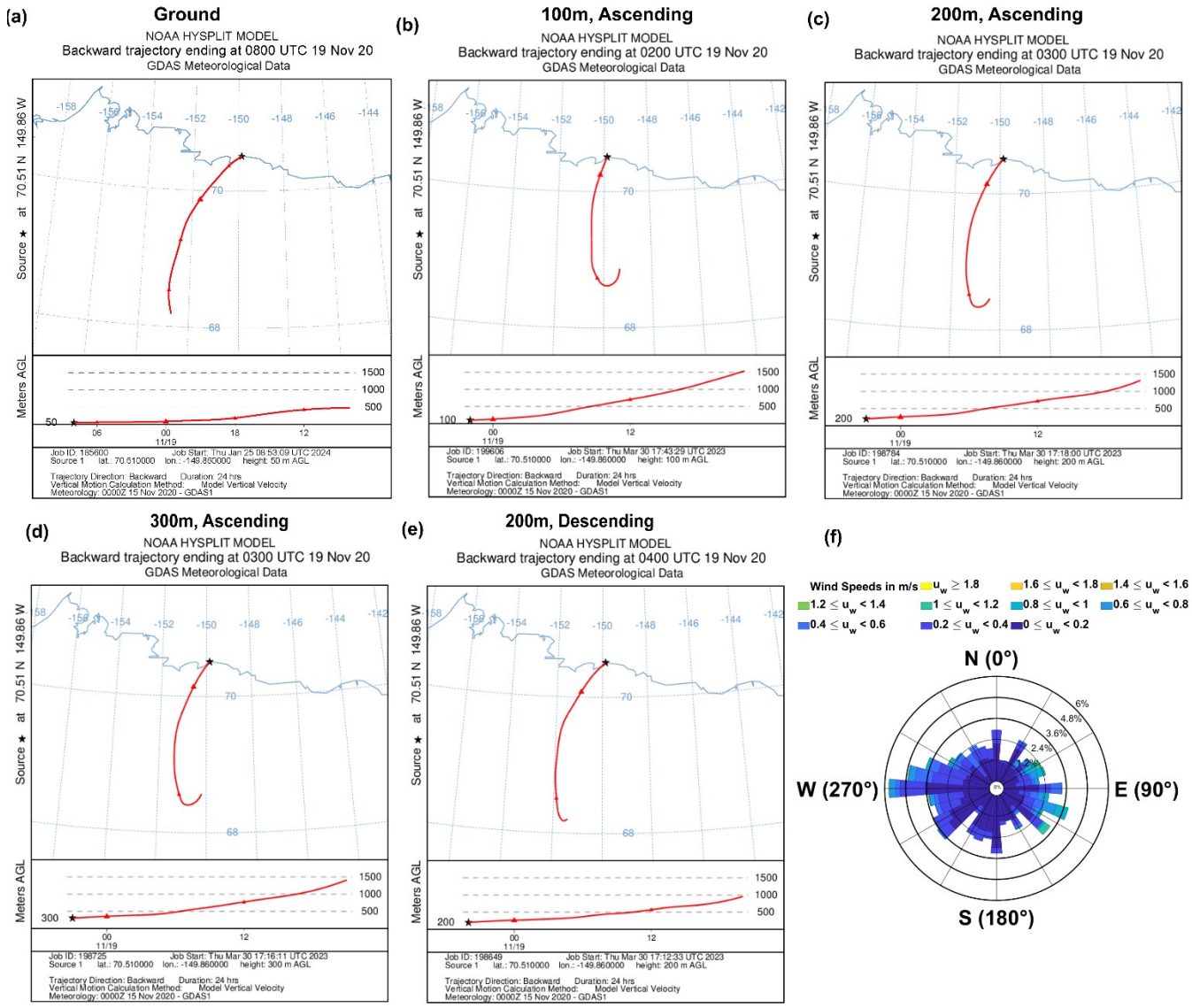


**Figure S1:** 24-hour HYSPLIT Back Trajectory analysis of the air masses during the sampling time on November 19, 2020. Here, image (a) shows the air masses source for ground particle sampling and images (b-e) show the air mass source for aloft particle sampling. (f) shows the wind rose plot.

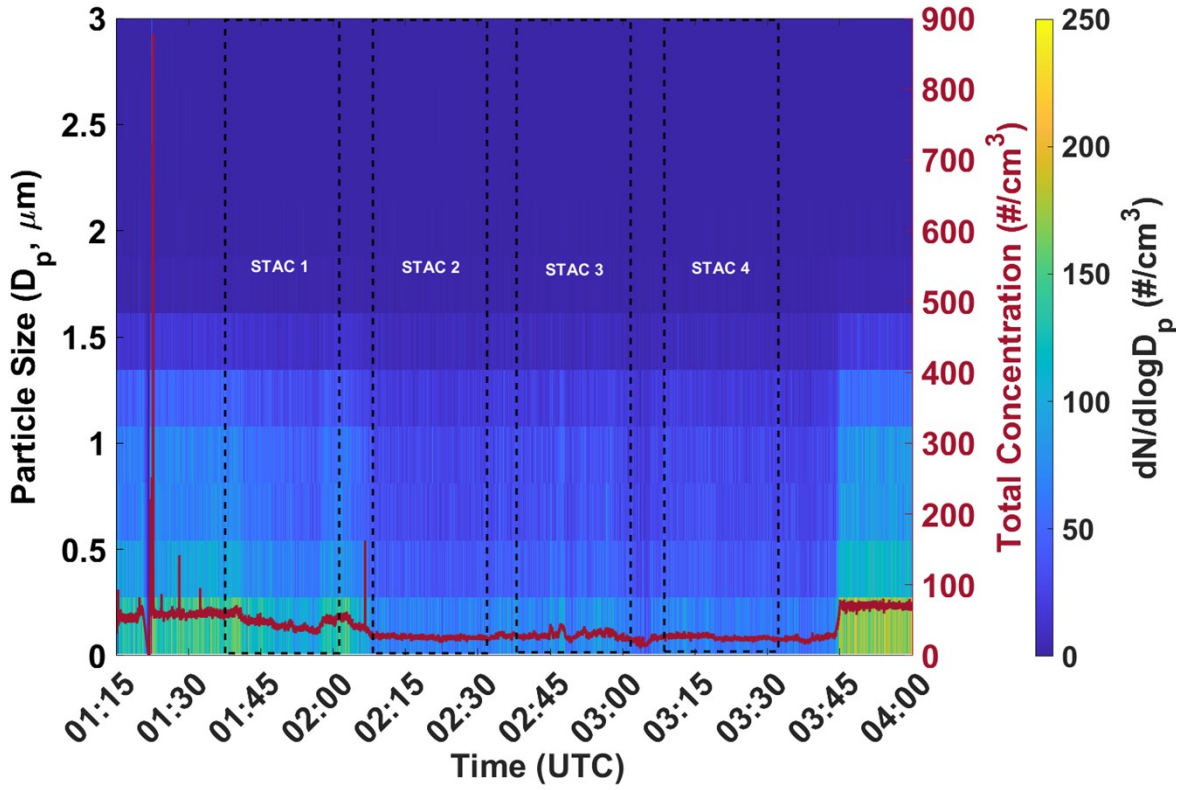


**Figure S2:** Particle concentration (maroon line) and size distribution from POPS.

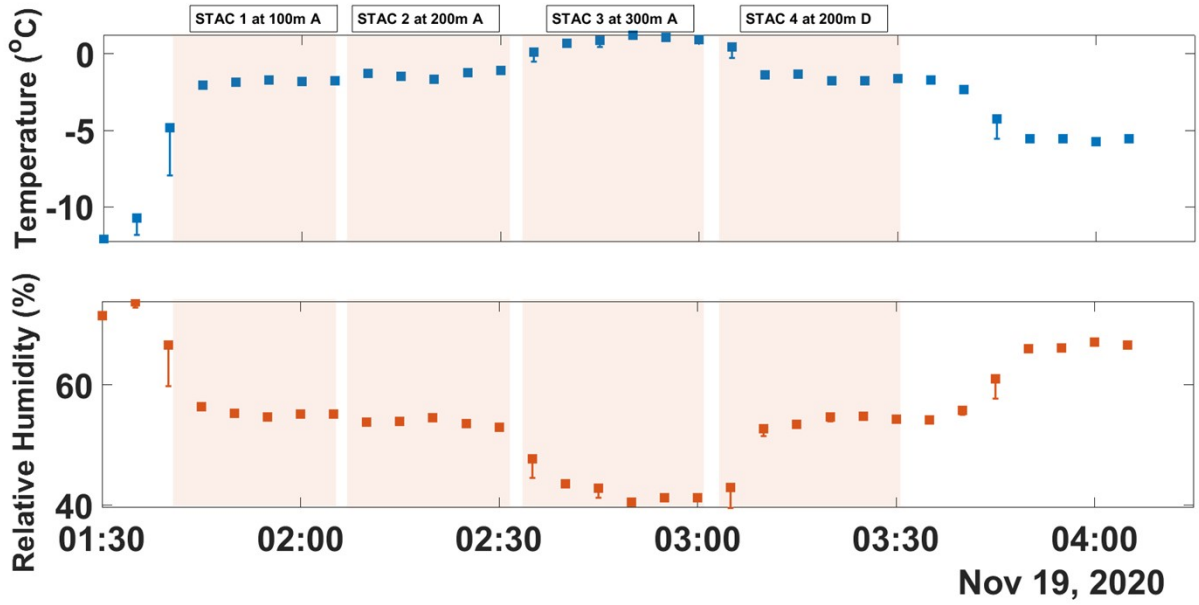


**Figure S3:** Five-minute means of temperature (top panel) and relative humidity (RH) (bottom panel) and. 'A' and 'D' indicates ascending and descending flights, respectively. The shaded region indicates the sampling time span at each altitude. The standard deviation at each sampling altitude is minimal for RH and temperature.

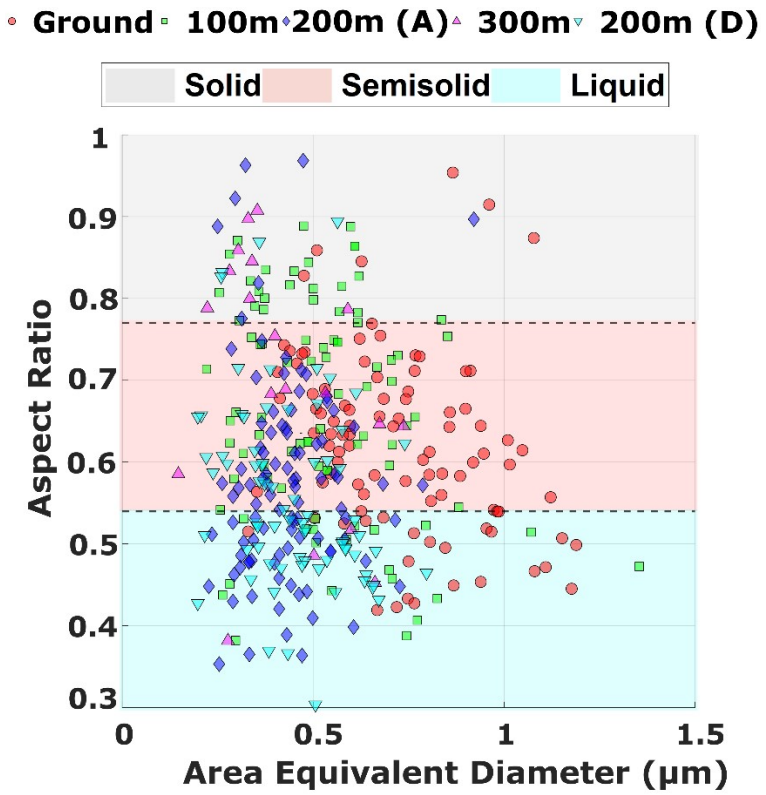


**Figure S4.** Scatter plot of particle aspect ratio versus area equivalent diameter (AED) for samples collected at different altitudes: Ground (red circles), 100m (green squares), 200m (A) (blue diamonds), 300m (magenta triangles), and 200m (D) (cyan inverted triangles). Horizontal dashed lines at aspect ratios of 0.54 and 0.77 delineate phase-state boundaries: particles with aspect ratios >0.77 are classified as solid (gray region), those between 0.54 and 0.77 as semi-solid (pink region), and those <0.54 as liquid (blue region).

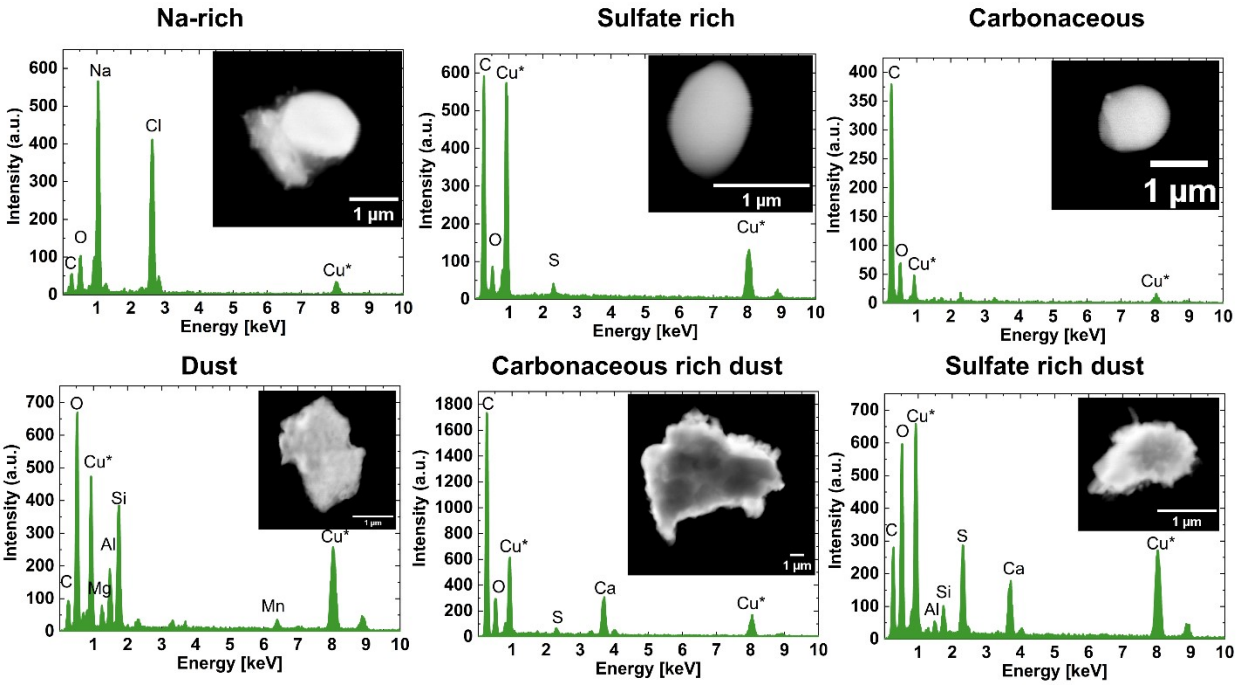


**Figure S5:** Representative SEM images and EDX spectra of major classes of particles.

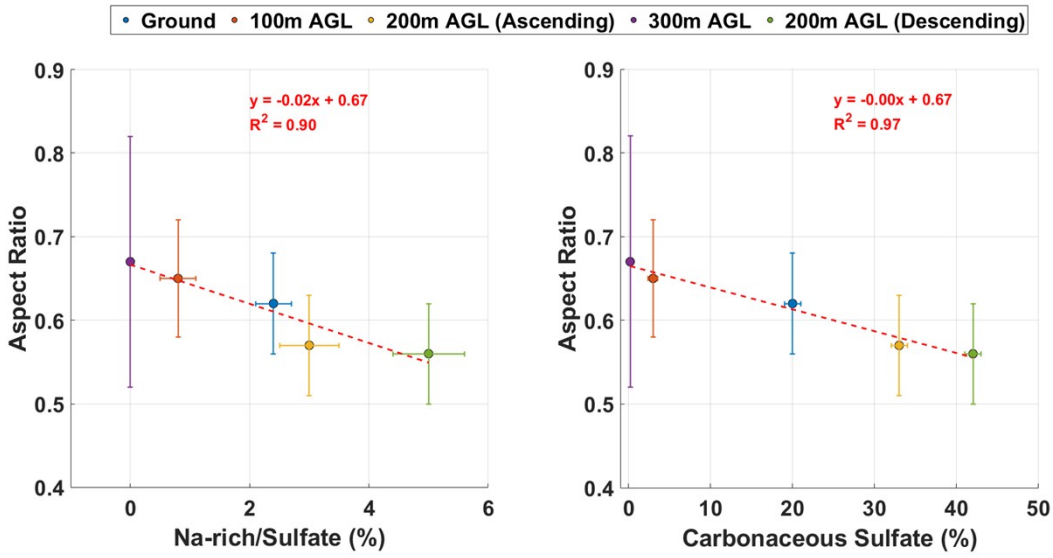


**Figure S6:** Relationship between aspect ratio and chemical composition at different altitudes. The left panel shows the linear relationship between aspect ratio and number fraction of Na-rich/Sulfate particles with a negative slope of -0.02 and $R^2$=0.90, indicating a strong correlation. The right panel illustrates the relationship between aspect ratio and number fraction of carbonaceous sulfate with a nearly flat slope of -0.00 and $R^2$=0.97, suggesting a strong but less steep correlation. Data points represent measurements taken at various altitudes: Ground, 100m AGL, 200m AGL (Ascending and Descending), and 300m AGL. Error bars indicate standard errors in the measurements.

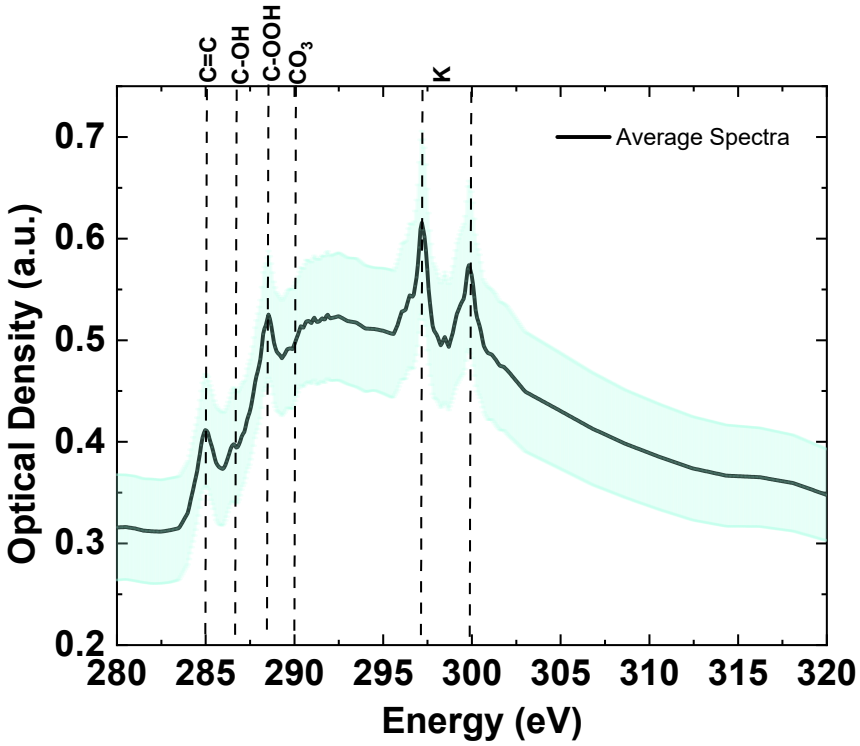


**Figure S7:** Mean STXM/NEXAFS spectrum of 19 individual particles collected from aloft at an altitude ranging from 100 m–300 m. The shaded region represents the variability (± standard deviation) among the NEXAFS spectra. Key absorption features correspond to carbon K-edge transitions, providing insights into the functional groups present in the sampled aerosols.

**Table S1**. Dates, times (UTC), flight hours, and altitudes during tethered balloon system flights and ground sampling.

| Impactor | UTC Date | Number of impactors | Altitude | Time (UTC) | Duration |
|---|---|---|---|---|---|
| STAC sampling with tethered ballon system flights | 11/19/2020 | STAC 1 | 100 m, A | 01:38–02:08 | 30 minutes |
| | | STAC 2 | 200 m, A | 02:09–02:39 | 30 minutes |
| | | STAC 3 | 300 m, A | 02:40–03:10 | 30 minutes |
| | | STAC 4 | 200 m, D | 03:11–03:41 | 30 minutes |
| Ground sampling with Sioutas Impactor | 11/19/2020 | Sioutas Personal Cascade Impactor | Above ground | 00:55–07:43 | 7 hours |

**Table S2.** Number of particles analyzed with CCSEM/EDX, STXM/NEXAFS and tilted Peltier stage in environmental scanning electron microscope. Percentage of particles in each of the classes are reported with standard error.

| Altitude | Ground | 100 m, A | 200 m, A | 300 m, A | 200 m, D |
|---|---|---|---|---|---|
| **Number of particles analyzed with CCSEM/EDX** | 2,164 | 803 | 1,167 | 491 | 1,496 |
| **Na-rich (%)** | 1.1 ±0.2 | 8 ±1 | 3.0 ±0.5 | 0.2 ±0.2 | 5.0 ±0.6 |
| **Na-rich/Sulfate (%)** | 2.4 ±0.3 | 0.8 ±0.3 | 3.0 ±0.5 | 0 | 5.0 ±0.6 |
| **Carbonaceous sulfate rich (%)** | 20 ±1 | 3.0±0.6 | 33 ±1 | 0.2 ±0.2 | 42 ±1 |
| **Carbonaceous rich (%)** | 71 ±1 | 88 ±1 | 58 ±1 | 77 ±2 | 45 ±1 |
| **Dust (%)** | 1.9 ±0.3 | 0.1 ±0.1 | 0.3 ±0.2 | 6 ±1 | 1.0 ±0.2 |
| **Carbonaceous coated dust (%)** | 0.5 ±0.2 | 0.3 ±0.2 | 1.0 ±0.2 | 15 ±2 | 0 |
| **Sulfate-coated dust (%)** | 1.9 ±0.3 | 0.4 ±0.2 | 0.3 ±0.2 | 0 | 0 |
| **Other (%)** | 1.3 ±0.2 | 0.3 ±0.2 | 1.0 ±0.3 | 2.1 ±0.7 | 2.0 ±0.4 |
| **Number of particles analyzed with STXM/NEXAFS** | 260 | 168 | 216 | 51 | 395 |
| **IN (%)** | 1.0±0.5 | 1.2 ±0.8 | 4.6 ±1.4 | 0 | 4.9 ±1.1 |
| **OC (%)** | 17 ±2 | 9 ±2 | 8 ±2 | 47 ±7 | 20 ±2 |
| **OC+EC (%)** | 10 ±2 | 6 ±1.8 | 3 ±1 | 20 ±6 | 4 ±1 |
| **OC+IN (%)** | 45 ±3 | 79 ±3 | 78 ±3 | 24 ±6 | 61 ±3 |
| **OC+EC+IN (%)** | 27±3 | 5.4±1.7 | 6±2 | 9±4 | 10±2 |
| **Number of particles analyzed with tilted Peltier stage** | 95 | 90 | 97 | 19 | 65 |
| **Solid (%)** | 7 ±3 | 28 ±5 | 7 ±3 | 42 ±11 | 6 ±3 |
| **Semi-solid (%)** | 66 ±5 | 50 ±5 | 50 ±5 | 37 ±11 | 58 ±6 |
| **Liquid (%)** | 26 ±5 | 22 ±4 | 43 ±5 | 21 ±9 | 36 ±6 |

**Table S3.** Mean (and standard deviation) RH and temperatures, as well as portable optical particle spectrometer (POPS) (0.13–3 μm) number concentrations, at different altitudes.

| Particle sample | RH (%) | Temperature (°C) | POPS Concentration (#/cm$^3$) |
|---|---|---|---|
| 100 m, A | 56 ±1 | -1.9 ±0.1 | 45 ±6 |
| 200 m, A | 54 ±1 | -1.4 ±0.2 | 25 ±2 |
| 300 m, A | 42 ±2 | 0.9 ±0.3 | 27 ±6 |
| 200 m, D | 54 ±1 | -1.6 ±0.2 | 25 ±2 |

**Table S4. Aspect ratio measured from the SEM images using ImageJ software**[11]**.**

| Ground | At 100m AGL | At 200m AGL (Ascending) | At 300m AGL | At 200m AGL (Descending) |
|---|---|---|---|---|

| Ground | At 100m AGL | At 200m AGL (Ascending) | At 300m AGL | At 200m AGL (Descending) |
|---|---|---|---|---|
| 0.954 | 0.888 | 0.968 | 0.859 | 0.874 |
| 0.915 | 0.888 | 0.963 | 0.833 | 0.869 |
| 0.874 | 0.871 | 0.922 | 0.799 | 0.832 |
| 0.859 | 0.864 | 0.897 | 0.788 | 0.780 |
| 0.845 | 0.864 | 0.888 | 0.786 | 0.684 |
| 0.669 | 0.711 | 0.605 | | 0.580 |
| 0.828 | 0.854 | 0.765 | 0.752 | 0.684 |
| 0.665 | 0.709 | 0.600 | | 0.571 |
| 0.769 | 0.844 | 0.732 | 0.740 | 0.683 |
| 0.665 | 0.709 | 0.600 | | 0.568 |
| 0.754 | 0.835 | 0.710 | 0.719 | 0.675 |
| 0.664 | 0.708 | 0.600 | | 0.565 |
| 0.751 | 0.833 | 0.703 | 0.715 | 0.660 |
| 0.661 | 0.707 | 0.589 | | 0.552 |
| 0.743 | 0.827 | 0.695 | 0.664 | 0.650 |
| 0.660 | 0.704 | 0.584 | | 0.541 |
| 0.736 | 0.821 | 0.682 | 0.660 | 0.646 |
| 0.656 | 0.697 | 0.583 | | 0.535 |
| 0.734 | 0.812 | 0.679 | 0.659 | 0.644 |
| 0.653 | 0.695 | 0.578 | | 0.531 |
| 0.732 | 0.798 | 0.678 | 0.629 | 0.639 |
| 0.650 | 0.692 | 0.578 | | 0.530 |
| 0.730 | 0.786 | 0.675 | 0.627 | 0.638 |
| 0.644 | 0.691 | 0.575 | | 0.528 |
| 0.729 | 0.783 | 0.662 | 0.578 | 0.636 |
| 0.723 | 0.774 | 0.657 | 0.520 | 0.636 |
| 0.721 | 0.763 | 0.652 | 0.492 | 0.623 |
| 0.712 | 0.762 | 0.643 | 0.462 | 0.609 |
| 0.711 | 0.757 | 0.643 | 0.397 | 0.602 |
| 0.711 | 0.756 | 0.641 | | 0.597 |
| 0.710 | 0.751 | 0.630 | | 0.595 |
| 0.704 | 0.744 | 0.628 | | 0.592 |
| 0.689 | 0.738 | 0.626 | | 0.590 |
| 0.686 | 0.730 | 0.625 | | 0.590 |
| 0.683 | 0.728 | 0.621 | | 0.589 |
| 0.678 | 0.715 | 0.620 | | 0.587 |
| 0.677 | 0.714 | 0.612 | | 0.587 |
| 0.677 | 0.711 | 0.609 | | 0.584 |

| | | | |
|---|---|---|---|
| 0.644 | 0.690 | 0.574 | 0.527 |
| 0.644 | 0.685 | 0.574 | 0.524 |
| 0.643 | 0.683 | 0.573 | 0.524 |
| 0.635 | 0.671 | 0.571 | 0.524 |
| 0.634 | 0.666 | 0.569 | 0.520 |
| 0.634 | 0.659 | 0.568 | 0.518 |
| 0.633 | 0.641 | 0.568 | 0.514 |
| 0.627 | 0.636 | 0.567 | 0.514 |
| 0.620 | 0.636 | 0.567 | 0.507 |
| 0.620 | 0.633 | 0.565 | 0.505 |
| 0.615 | 0.627 | 0.564 | 0.501 |
| 0.613 | 0.624 | 0.557 | 0.500 |
| 0.612 | 0.618 | 0.555 | 0.499 |
| 0.610 | 0.617 | 0.549 | 0.498 |
| 0.603 | 0.611 | 0.547 | 0.497 |
| 0.600 | 0.611 | 0.542 | 0.493 |
| 0.600 | 0.610 | 0.541 | 0.490 |
| 0.597 | 0.609 | 0.533 | 0.487 |
| 0.586 | 0.609 | 0.533 | 0.486 |
| 0.586 | 0.608 | 0.532 | 0.483 |
| 0.585 | 0.601 | 0.532 | 0.482 |
| 0.584 | 0.599 | 0.530 | 0.478 |
| 0.583 | 0.587 | 0.529 | 0.478 |
| 0.577 | 0.586 | 0.528 | 0.473 |
| 0.575 | 0.586 | 0.522 | 0.471 |
| 0.573 | 0.582 | 0.520 | 0.466 |
| 0.564 | 0.582 | 0.515 | 0.465 |
| 0.561 | 0.575 | 0.512 | 0.460 |

| Ground | At 100m AGL | At 200m AGL (Ascending) | At 300m AGL | At 200m AGL (Descending) |
|---|---|---|---|---|
| 0.553 | 0.544 | 0.509 | | 0.452 |
| 0.542 | 0.541 | 0.506 | | 0.443 |
| 0.540 | 0.532 | 0.500 | | 0.439 |
| 0.540 | 0.531 | 0.496 | | 0.385 |
| 0.540 | 0.525 | 0.496 | | 0.382 |
| 0.532 | 0.524 | 0.493 | | 0.322 |
| 0.532 | 0.521 | 0.492 | | 0.457 |
| 0.528 | 0.520 | 0.487 | | 0.452 |

| | | |
|---|---|---|
| 0.525 | 0.520 | 0.486 |
| 0.519 | 0.517 | 0.485 |
| 0.515 | 0.509 | 0.485 |
| 0.515 | 0.506 | 0.484 |
| 0.513 | 0.480 | 0.479 |
| 0.507 | 0.476 | 0.471 |
| 0.502 | 0.467 | 0.467 |
| 0.499 | 0.461 | 0.459 |
| 0.495 | 0.454 | 0.458 |
| 0.479 | 0.449 | 0.458 |
| 0.472 | 0.445 | 0.452 |
| 0.467 | 0.420 | 0.449 |
| 0.454 | 0.403 | 0.447 |
| 0.449 | 0.397 | 0.441 |
| 0.445 | 0.573 | 0.433 |
| 0.433 | 0.564 | 0.423 |
| 0.427 | | 0.413 |
| 0.423 | | 0.404 |
| 0.419 | | 0.381 |
| 0.56 | | 0.380 |
| 0.557 | | 0.370 |
| | | 0.511 |
| | | 0.509 |

## References


1 N. N. Lata, B. Zhang, S. Schum, L. Mazzoleni, R. Brimberry, M. A. Marcus, W. H. Cantrell, P. Fialho, C. Mazzoleni and S. China, *ACS Earth Space Chem.*, 2021, **5**, 3499–3510.

2 A. L. D. Kilcoyne, T. Tyliszczak, W. F. Steele, S. Fakra, P. Hitchcock, K. Franck, E. Anderson, B. Harteneck, E. G. Rightor, G. E. Mitchell, A. P. Hitchcock, L. Yang, T. Warwick and H. Ade, *J Synchrotron Rad*, 2003, **10**, 125–136.

3 R. C. Moffet, T. Henn, A. Laskin and M. K. Gilles, *Anal. Chem.*, 2010, **82**, 7906–7914.

4 R. J. Hopkins, A. V. Tivanski, B. D. Marten and M. K. Gilles, *Journal of Aerosol Science*, 2007, **38**, 573–591.

5 A. V. Tivanski, R. J. Hopkins, T. Tyliszczak and M. K. Gilles, *J. Phys. Chem. A*, 2007, **111**, 5448–5458.

6 R. C. Moffet, A. V. Tivanski and M. K. Gilles, *Signorell, R., Reid, JP, Eds*, 2010, 243–272.

7 M. Fraund, T. Park, L. Yao, D. Bonanno, D. Q. Pham and R. C. Moffet, *Atmospheric Measurement Techniques*, 2019, **12**, 1619–1633.

8 R. E. O'Brien, B. Wang, A. Laskin, N. Riemer, M. West, Q. Zhang, Y. Sun, X.-Y. Yu, P. Alpert, D. A. Knopf, M. K. Gilles and R. C. Moffet, *Journal of Geophysical Research: Atmospheres*, 2015, **120**, 9591–9605.

9 B. L. Henke, E. M. Gullikson and J. C. Davis, *Atomic Data and Nuclear Data Tables*, 1993, **54**, 181–342.

10 R. E. O'Brien, A. Neu, S. A. Epstein, A. C. MacMillan, B. Wang, S. T. Kelly, S. A. Nizkorodov, A. Laskin, R. C. Moffet and M. K. Gilles, *Geophysical Research Letters*, 2014, **41**, 4347–4353.

11 T. J. Collins, *BioTechniques*, 2007, **43**, S25–S30.